Medical Physics
The International Journal of Medical Physics Research and Practice

Patient-bounded extrapolation using low-dose priors for volume-of-interest imaging in C-arm CT

Y. Xia, S. Bauer, A. Maier, M. Berger, and J. Hornegger

Citation: Medical Physics **42**, 1787 (2015); doi: 10.1118/1.4914135
View online: http://dx.doi.org/10.1118/1.4914135
View Table of Contents: http://scitation.aip.org/content/aapm/journal/medphys/42/4?ver=pdfcov
Published by the American Association of Physicists in Medicine

Patient-bounded extrapolation using low-dose priors for volume-of-interest imaging in C-arm CT

Y. Xia[a)]
Pattern Recognition Lab, Friedrich-Alexander-University Erlangen-Nuremberg, Erlangen 91058, Germany

S. Bauer
Siemens AG, Healthcare Sector, Forchheim 91301, Germany

A. Maier, M. Berger, and J. Hornegger[a)]
Pattern Recognition Lab, Friedrich-Alexander-University Erlangen-Nuremberg, Erlangen 91058, Germany

(Received 2 September 2014; revised 29 November 2014; accepted for publication 11 December 2014; published 20 March 2015)

Purpose: Three-dimensional (3D) volume-of-interest (VOI) imaging with C-arm systems provides anatomical information in a predefined 3D target region at a considerably low x-ray dose. However, VOI imaging involves laterally truncated projections from which conventional reconstruction algorithms generally yield images with severe truncation artifacts. Heuristic based extrapolation methods, e.g., water cylinder extrapolation, typically rely on techniques that complete the truncated data by means of a continuity assumption and thus appear to be *ad-hoc*. It is our goal to improve the image quality of VOI imaging by exploiting existing patient-specific prior information in the workflow.
Methods: A necessary initial step prior to a 3D acquisition is to isocenter the patient with respect to the target to be scanned. To this end, low-dose fluoroscopic x-ray acquisitions are usually applied from anterior–posterior (AP) and medio-lateral (ML) views. Based on this, the patient is isocentered by repositioning the table. In this work, we present a patient-bounded extrapolation method that makes use of these noncollimated fluoroscopic images to improve image quality in 3D VOI reconstruction. The algorithm first extracts the 2D patient contours from the noncollimated AP and ML fluoroscopic images. These 2D contours are then combined to estimate a volumetric model of the patient. Forward-projecting the shape of the model at the eventually acquired C-arm rotation views gives the patient boundary information in the projection domain. In this manner, we are in the position to substantially improve image quality by enforcing the extrapolated line profiles to end at the known patient boundaries, derived from the 3D shape model estimate.
Results: The proposed method was evaluated on eight clinical datasets with different degrees of truncation. The proposed algorithm achieved a relative root mean square error (rRMSE) of about 1.0% with respect to the reference reconstruction on nontruncated data, even in the presence of severe truncation, compared to a rRMSE of 8.0% when applying a state-of-the-art heuristic extrapolation technique.
Conclusions: The method we proposed in this paper leads to a major improvement in image quality for 3D C-arm based VOI imaging. It involves no additional radiation when using fluoroscopic images that are acquired during the patient isocentering process. The model estimation can be readily integrated into the existing interventional workflow without additional hardware. [http://dx.doi.org/10.1118/1.4914135]

Key words: computed tomography, volume of interest imaging, truncation correction, extrapolation, fluoroscopic image

1. INTRODUCTION

Three-dimensional (3D) C-arm based volume-of-interest (VOI) imaging is a valuable tool in interventional radiology for therapy planning and guidance. It is capable of providing 3D anatomical information in a predefined target region at considerably low x-ray dose. In neurointerventions, some applications only require a small VOI to be imaged, e.g., examination of a deployed stent or coil, resulting in severe truncation of the projection data. However, conventional reconstruction algorithms generally yield images with heavy truncation artifacts from these laterally severely truncated projections.[1] Such artifacts manifest as cupping-like effects and incorrect Hounsfield unit (HU) values.

So far, various approaches concerning the correction of truncation have been proposed in the literature. A major category among these methods is based on estimating the missing data using a heuristic extrapolation procedure: Ohnesorge *et al.*[2] used a symmetric mirroring extrapolation scheme to reduce the truncation artifacts from objects extending outside the measured field of view (FOV). Hsieh *et al.*[3] suggested a method that approximates the missing measurements by integrals along parallel rays through a 2D water cylinder. Some functions that fit the missing portion of the patient, such as

a square root function or a Gaussian function, also have been investigated by Sourbelle *et al.*[4] and Zellerhoff *et al.*[5] Although these methods can be carried out without *a priori* information, they rely on heuristics. The degree of accuracy of these extrapolation estimates highly depends on the level of truncation. They may be difficult to correct for the severe truncations that could be encountered in VOI scans.

Later, Maltz *et al.*[6] observed that the thickness of the patient could be estimated by calculating water-equivalent thicknesses from the measured attenuation profiles, so that the unknown patient boundary can be approximated. However, in practice, the presence of any nonwater tissue (air, bond, or metal implants) might result in a substantial over/under-estimation of the actual object thickness.

In contrast, Ruchala *et al.*,[7] Wiegert *et al.*,[8] and Kolditz *et al.*[9] suggested that patient size and shape information can be obtained from an *a priori* low-dose CT scan, if available. By forward-projection of this *a priori* CT volume, the collimated regions in the VOI acquisition can be extended in an accurate manner. These additional scans, however, may interrupt the interventional workflow and cost extra radiation dose to the patient. Also, additional registration step is required due to repositioning of the patient between two scans. Alternatively, Sen Sharma *et al.*[10] suggested acquiring an additional scan but with only a small set of nontruncated projections. Then, interpolation and extrapolation steps are applied on this sparse set of nontruncated projections, followed by a combination with the subsequently acquired truncated projection data in the sinogram domain. The image quality of reconstructions, however, highly depends on the number of nontruncated projections. Yu *et al.*[11] developed a VOI/ROI reconstruction scheme that is able to use two global nontruncated projections to cope with truncation artifacts. But the method was based on compressed sensing iterative techniques.

Chityala *et al.*,[12] Chen *et al.*,[13] and Schafer *et al.*[14] proposed a different method that irradiates parts of the scan FOV at a lower dose. In this case, a nonuniform VOI beam filter is applied to reduce dose outside the VOI. Therefore, projections will not be truncated, but data acquisition might become less flexible due to the fixed VOI size and filter thickness. Moreover, dose reduction benefits may also be reduced compared to the fully truncated data.

Dennerlein and Maier[15] reformulated the Feldkamp–Davis–Kress (FDK) algorithm[16] into a reconstruction scheme that is less sensitive to transaxial data truncation. For this purpose, the standard high-pass ramp filter was decomposed into a local Laplace filter and a nonlocal low-pass filter. Although the method is robust to severe truncation, a global scaling/offset artifact is typically observed in the reconstruction volume that has to be compensated (Xia *et al.*[17]).

Although it has been proven that reconstructions from severely truncated data yield no unique solution in general, a theoretically exact solution has been developed by Ye *et al.*,[18] Kudo *et al.*,[19] Yu *et al.*,[20,21] and Yang *et al.*,[22] namely, interior tomography, based on the idea of differentiate backprojection (DBP) with different *a priori* knowledge on a ROI. Such knowledge could be a known subregion inside a ROI (Ye *et al.*[18] and Kudo *et al.*[19]) or a sparsity model of a ROI (Yu *et al.*,[20,21] Yang *et al.*,[22] and Katsevich *et al.*[23]). Then, a projection onto convex sets (POCS) algorithm or total variation (TV) based compressed sensing was used to reconstruct images from fully truncated data, depending on which *a priori* information is available.

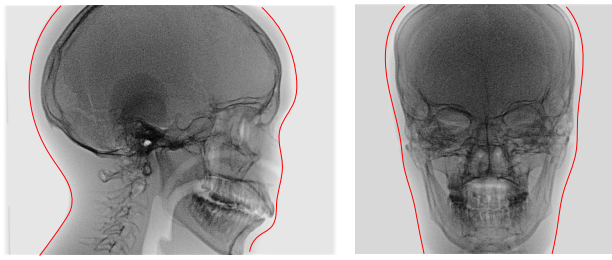

FIG. 1. Illustration of fluoroscopic x-ray projections from medio-lateral view and anterior–posterior view, respectively. They require considerably low x-ray dose and are usually applied prior to a 3D scan, to examine if the diagnostic VOI is optimally centered. The red outlines indicate the extracted boundary information.

In this paper, we present a patient-bounded extrapolation method that leads to major improvements in the accuracy of 3D VOI imaging, even in the presence of severely truncated data. The method does not require any additional hardware and can be readily integrated into the existing interventional workflow. It is based on the fact that prior to a 3D scan, two fluoroscopic x-ray acquisitions are generally performed from anterior–posterior (AP) and medio-lateral (ML) views, to isocenter the patient with respect to the target to be scanned, see Fig. 1. These fluoroscopic acquisitions require considerably low x-ray dose. The fundamental idea of the proposed method is to estimate a 3D shape model of the patient from these low-dose nontruncated fluoroscopic images and then exploit this patient-specific *a priori* shape knowledge for the extrapolation of truncated projections.

2. METHODS

This section starts with an overview of the proposed patient-bounded extrapolation method, which consists of the following steps. First, we estimate the rough 3D patient shape based on two fluoroscopic projections, using per-slice ellipse fitting. Forward-projecting this 3D model for any projection angle acquired during the actual VOI scan gives the patient bounded information for the corresponding projection. Then, detruncated projection data could be obtained by adapting the extrapolated profile to fit the known profile boundary points. The flowchart of the algorithm is illustrated in Fig. 2. The details are elaborated in Secs. 2.A–2.E; also see Fig. 3 for notations.

2.A. Patient shape model estimation using slice-wise ellipse

The first step is to extract the boundaries from fluoroscopic images shown as the red outlines in Fig. 1. Here, we

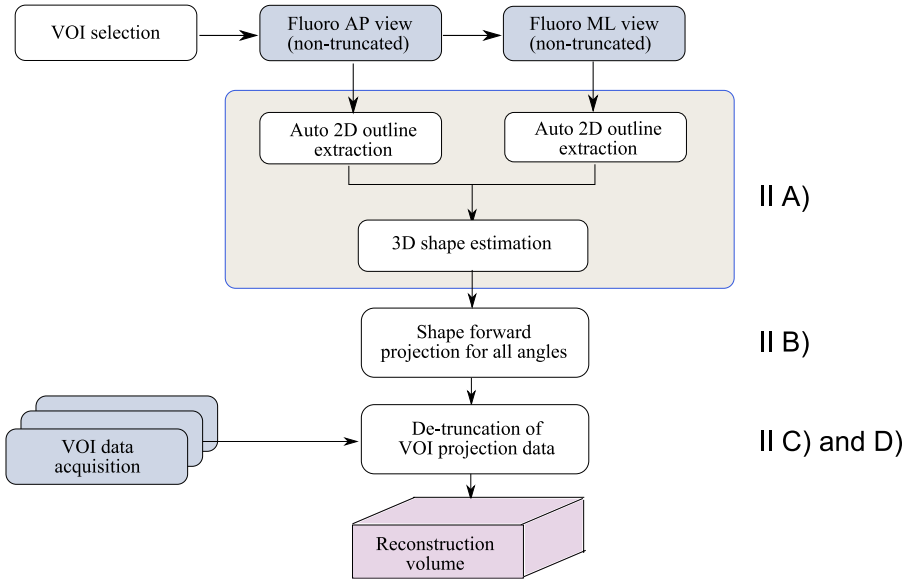

FIG. 2. Flowchart of the proposed patient boundary extrapolation procedure.

can readily detect the edges by using an empirically preset air/tissue threshold. Suppose, $\mathbf{u}_{\text{lb}}^{\text{AP}} = (u_{\text{lb}}^{\text{AP}}, v_i, 1)$, $\mathbf{u}_{\text{rb}}^{\text{AP}}$, $\mathbf{u}_{lb}^{\text{ML}}$, and $\mathbf{u}_{\text{rb}}^{\text{ML}}$ are the homogeneous coordinates of the segmented left and right boundary points at detector row v_i of the 2D fluoroscopic images from AP and ML view. Let $\mathbf{P}^{\lambda} \in \mathbb{R}^{3\times4}$ be the projection matrix at the C-arm rotation angle λ that maps position $\mathbf{x} = [x, y, z]$ in the C-arm coordinate frame to a position $\mathbf{u} = [\omega u, \omega v, \omega]$ in the 2D projection plane

$$\mathbf{u} = \mathbf{P}^{\lambda} \begin{bmatrix} \mathbf{x} \\ 1 \end{bmatrix}. \tag{1}$$

The matrix $\mathbf{P}^{\lambda}$ can be decomposed as follows:

$$\mathbf{P}^{\lambda} = \left[\mathbf{P}_{13}^{\lambda} \,|\, \mathbf{p}_4^{\lambda}\right] = [\mathbf{AR} \,|\, \mathbf{At}], \tag{2}$$

where $\mathbf{R} \in \mathbb{R}^{3\times3}$ denotes the rotation matrix, $\mathbf{t} \in \mathbb{R}^3$ denotes the translation vector, and $\mathbf{A} \in \mathbb{R}^{3\times3}$ the intrinsic parameter matrix.

Then, we can compute the direction unit vector $\mathbf{e}_m^{\text{AP}}$, $\mathbf{e}_m^{\text{ML}}$ of the ray that connects the source to the middle point of the two boundaries, i.e., $\mathbf{u}_m^{\text{AP}} = (\mathbf{u}_{\text{lb}}^{\text{AP}} + \mathbf{u}_{\text{rb}}^{\text{AP}})/2$ and $\mathbf{u}_m^{\text{ML}} = (\mathbf{u}_{\text{lb}}^{\text{ML}} + \mathbf{u}_{\text{rb}}^{\text{ML}})/2$ as

$$\mathbf{e}_m^{\text{AP}} = \frac{(\mathbf{P}_{13}^{\text{AP}})^{-1}\mathbf{u}_m^{\text{AP}}}{\|(\mathbf{P}_{13}^{\text{AP}})^{-1}\mathbf{u}_m^{\text{AP}}\|_2}, \qquad \mathbf{e}_m^{\text{ML}} = \frac{(\mathbf{P}_{13}^{\text{ML}})^{-1}\mathbf{u}_m^{\text{ML}}}{\|(\mathbf{P}_{13}^{\text{ML}})^{-1}\mathbf{u}_m^{\text{ML}}\|_2}, \tag{3}$$

where $\mathbf{P}^{-1}$ denotes the pseudo-inverse of the matrix $\mathbf{P}$.

Now the ray equations can be expressed as

$$\mathbf{l}_m^{\text{AP}}(t) = \mathbf{s}^{\text{AP}} + t\mathbf{e}_m^{\text{AP}} \quad \text{and} \quad \mathbf{l}_m^{\text{ML}}(l) = \mathbf{s}^{\text{ML}} + l\mathbf{e}_m^{\text{ML}}, \tag{4}$$

where $\mathbf{s}^{\text{AP}}$ and $\mathbf{s}^{\text{ML}}$ denote the x-ray source positions at AP and ML views, which can be computed using $\mathbf{s} = -\mathbf{P}_{13}^{-1}\mathbf{p}_4$ and $t, l \in \mathbb{R}$.

Then, the center of the fitted ellipse $\mathbf{x}_0$ is estimated by computing the intersection of the two rays $\mathbf{l}_m^{\text{AP}}$ and $\mathbf{l}_m^{\text{ML}}$. Here, we confine to breaking the problem down to a 2D line intersection by setting the third component of the 3D lines to zero, i.e., $\mathbf{s}^{\text{AP}}\mathbf{I}_z = \mathbf{s}^{\text{ML}}\mathbf{I}_z = 0$ and $\mathbf{e}_m^{\text{AP}}\mathbf{I}_z = \mathbf{e}_m^{\text{ML}}\mathbf{I}_z = 0$, where $\mathbf{I}_z = [0 \quad 0 \quad 1]^T$. The reason to make such an approximation is that we only need to compute the u-axis coordinates of the object boundary in the forward projection procedure. The v-axis coordinates are already given as the detector row indexes where we extracted the outline information, i.e., v_i. Then, the

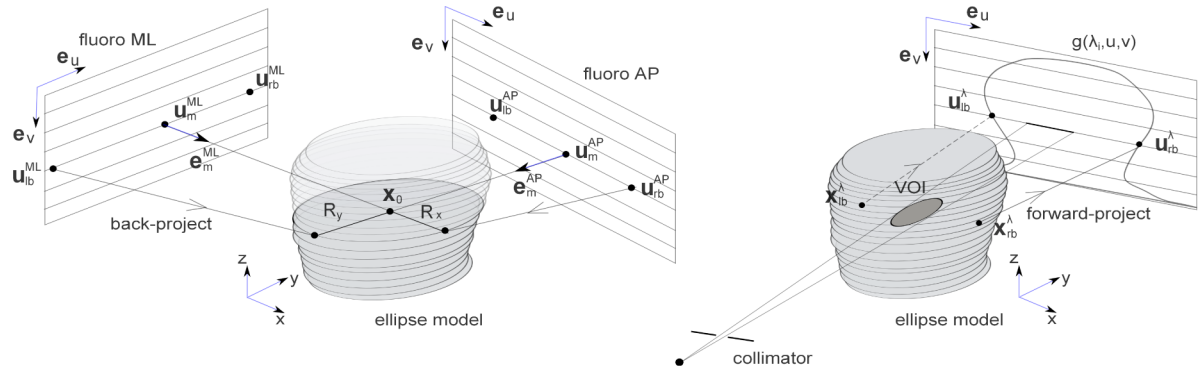

FIG. 3. Illustration of the patient-bounded extrapolation scheme. (Left) Contour-bounded slice-wise ellipse fitting. (Right) Forward-projection of the boundaries of the previously estimated patient shape model at a given C-arm rotation view provides the patient boundary in the projection domain.

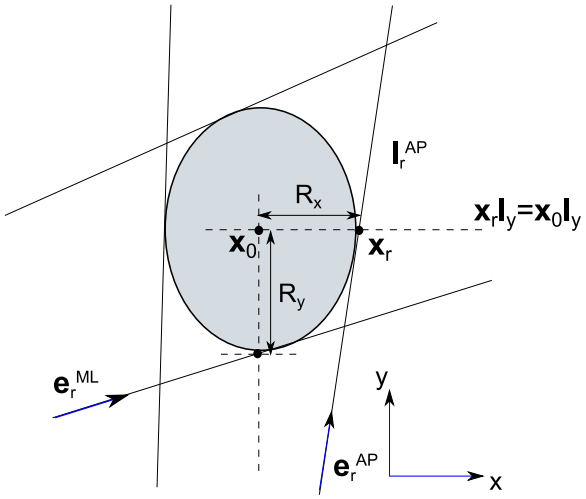

FIG. 4. Illustration of how to approximate the ellipse radii R_x and R_y. To estimate R_x for instance, we need to compute the x-axis distance between $\mathbf{x}_0$ and $\mathbf{x}_r$ (a point located on the line $\mathbf{l}_r^{AP}$ that has the same y-axis coordinate as $\mathbf{x}_0$). Such an approximation is valid due to the small fan angle in C-arm system.

problem is to solve the intersection of the following 2D line equations:

$$\begin{cases} y = ax + b \\ y = cx + d \end{cases}, \tag{5}$$

with

$$a = \frac{\mathbf{e}_m^{ML}\mathbf{I}_y}{\mathbf{e}_m^{ML}\mathbf{I}_x},\ b = \mathbf{s}^{ML}\mathbf{I}_y - a\mathbf{s}^{ML}\mathbf{I}_x,$$
$$c = \frac{\mathbf{e}_m^{AP}\mathbf{I}_y}{\mathbf{e}_m^{AP}\mathbf{I}_x},\ d = \mathbf{s}^{AP}\mathbf{I}_y - a\mathbf{s}^{AP}\mathbf{I}_x, \tag{6}$$

where $\mathbf{I}_x = \begin{bmatrix}1 & 0 & 0\end{bmatrix}^T$ and $\mathbf{I}_y = \begin{bmatrix}0 & 1 & 0\end{bmatrix}^T$.

So far, we computed the first two components of the intersection point $\mathbf{x}_0$. To establish a 3D model in the volume domain, the third component of $\mathbf{x}_0$ can be approximated by the third component of the closest point between the two 3D lines $\mathbf{l}_m^{AP}$ and $\mathbf{l}_m^{ML}$, which is given by

$$\mathbf{x}_0\mathbf{I}_z := \mathbf{x}_{clo}\mathbf{I}_z \tag{7}$$

with the closest point determined by (see Appendix for the derivation)

$$\mathbf{x}_{clo} = \mathbf{s}^{AP} + \frac{\left((\mathbf{s}^{ML} - \mathbf{s}^{AP}) \times \mathbf{e}_m^{ML}\right) \cdot \left(\mathbf{e}_m^{AP} \times \mathbf{e}_m^{ML}\right)}{\left\|\mathbf{e}_m^{AP} \times \mathbf{e}_m^{ML}\right\|^2} \mathbf{e}_m^{AP}. \tag{8}$$

Now, we need to determine the radii R_x, R_y of the ellipse. The line equation of the rays from AP view that connects the patient boundary and source can also be expressed as (e.g., right boundary) $\mathbf{l}_r^{AP}(h) = \mathbf{s}^{AP} + h\mathbf{e}_r^{AP}$, where $\mathbf{e}_r^{AP}$ is computed using $\mathbf{u}_{rb}^{AP}$ similar to Eq. (3). Suppose, $\mathbf{x}_r$ is the point located on the line $\mathbf{l}_r^{AP}$ that satisfies $\mathbf{x}_r\mathbf{I}_y = \mathbf{x}_0\mathbf{I}_y$, i.e., with the same y-axis coordinate as $\mathbf{x}_0$; also see Fig. 4 for illustration. Then, the radius along the x-axis R_x can be approximated as follows:

$$R_x = (\mathbf{x}_r - \mathbf{x}_0)\mathbf{I}_x. \tag{9}$$

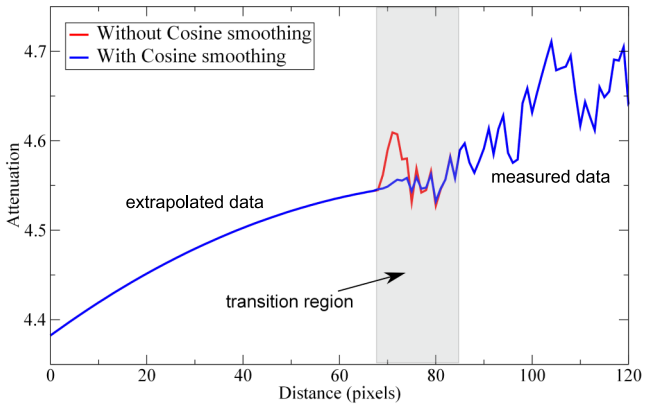

FIG. 5. Comparison of an extrapolated line with/without cosine smoothing in the transition region.

In analogy, we can use the boundary from ML view to determine the radius of the ellipse along the y-axis R_y.

So far, for each detector row v_i, we computed an associated ellipse that is used to approximate a slice of the patient outline in the volume domain. This ellipse is parametrized by the center $\mathbf{x}_0$ and two radii R_x and R_y.

2.B. Patient boundary estimation for arbitrary projections

With the estimated ellipse in the volumetric image domain, we can compute the left and right patient boundaries of that ellipse for any given C-arm rotation angle λ as follows:

$$\mathbf{x}_{lb}^{\lambda} = \mathbf{x}_0 - r\mathbf{e}_u, \tag{10}$$
$$\mathbf{x}_{rb}^{\lambda} = \mathbf{x}_0 + r\mathbf{e}_u, \tag{11}$$

where $r = \sqrt{(R_y \cos\lambda)^2 + (R_x \sin\lambda)^2}$ and $\mathbf{e}_u$ denotes the unit vector in detector row direction.

Then, we forward-project these voxel positions onto the 2D projection plane using Eq. (1), also cf. Fig. 3,

$$\mathbf{u}_{lb}^{\lambda} = \mathbf{P}^{\lambda}\begin{bmatrix}\mathbf{x}_{lb}^{\lambda} \\ 1\end{bmatrix} \quad \mathbf{u}_{rb}^{\lambda} = \mathbf{P}^{\lambda}\begin{bmatrix}\mathbf{x}_{rb}^{\lambda} \\ 1\end{bmatrix}. \tag{12}$$

The estimated patient left and right boundaries at the detector row v_i and rotation angle λ, i.e., (u_{lb}^{λ}, v_i) and (u_{rb}^{λ}, v_i), can be obtained with $u_{lb}^{\lambda} = \mathbf{u}_{lb}^{\lambda}\mathbf{I}_x / \mathbf{u}_{lb}^{\lambda}\mathbf{I}_z$ and $u_{rb}^{\lambda} = \mathbf{u}_{rb}^{\lambda}\mathbf{I}_x / \mathbf{u}_{rb}^{\lambda}\mathbf{I}_z$.

2.C. Bounded VOI projection profile extrapolation

Based on the estimated patient boundaries in the VOI scan projection data, we are in the position to apply any extrapolation technique and adapting it according to the restriction that the extrapolated profile must end at the known patient boundaries. In this paper, we adapt the water cylinder approach of Hsieh *et al.*[3] by expanding or compressing the initial extrapolated lines to fulfill this restriction. Let $g_{\lambda,v}(u)$ be the projection data at the given detector row v and rotation

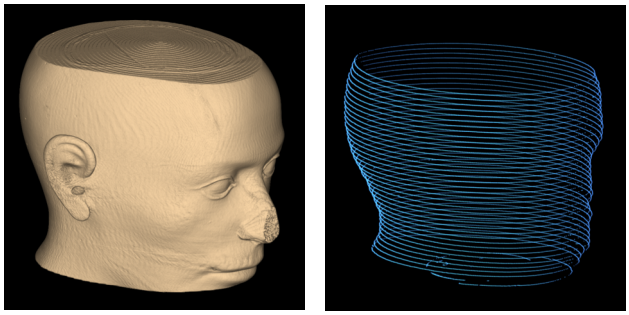

FIG. 6. Visualization of a head phantom shape extracted from the noncollimated 3D reconstruction (left) and the 3D volumetric model estimated from two orthogonal projections with different ellipses in each slice (right).

angle λ. Then, extrapolation is carried out row-wise as

$$\widetilde{g}^{\mathrm{wat}}_{\lambda,v}(u) = 2\mu\sqrt{R^2 - \xi^2(u-u_w)^2}, \tag{13}$$

where μ denotes the water attenuation coefficient, u_w denotes the location of the fitted cylinder with respect to the detector row, and R denotes the radius. As described in Hsieh's work,[3] the parameters u_w and R can be determined by

$$u_w = \frac{g_{\lambda,v}(u_t)\,g'_{\lambda,v}(u_t)}{4\mu^2}, \qquad R = \sqrt{\frac{g_{\lambda,v}(u_t)}{4\mu^2} + u_w^2}, \tag{14}$$

where u_t and $g'_{\lambda,v}(u_t)$ denote the truncation boundary position and slope of the truncation projection boundary samples, respectively.

In contrast to the formulation by Hsieh *et al.*, in Eq. (13), we introduce ξ that serves as a scaling factor to stretch or shrink the extrapolated profiles. The values of ξ can be computed by using the boundary index u_b (here, we do not distinguish the left or right boundary. Both are denoted as u_b) that we obtained in Sec. 2.B,

$$\xi^2 = \frac{R}{u_b - u_w}. \tag{15}$$

2.D. Bounded square root function extrapolation

As an alternative, we also investigate the square root function extrapolation that was proposed by Sourbelle *et al.*[4] For a given detector row v and rotation angle λ, the extrapolation function is provided as

$$\widetilde{g}^{\mathrm{sqr}}_{\lambda,v}(u) = \sqrt{\alpha\cdot u^2 + \beta\cdot u + \gamma}. \tag{16}$$

To determine the parameters α, β, and γ, the following continuity equations are used:

$$g_{\lambda,v}(u_t) = \sqrt{\alpha\cdot u_t^2 + \beta\cdot u_t + \gamma}, \tag{17}$$

$$g'_{\lambda,v}(u_t) = \frac{\beta + 2\alpha\cdot u_t}{2g_{\lambda,v}(u_t)}, \tag{18}$$

where u_t and $g'_{\lambda,v}(u_t)$ denote the position and slope of the truncation edge, respectively.

We integrate the patient boundary information into Eq. (16) such that the extrapolated profile ends at u_b,

$$g_{\lambda,v}(u_b) = \sqrt{\alpha\cdot u_b^2 + \beta\cdot u_b + \gamma} = 0. \tag{19}$$

Thus, the three parameters α, β, and γ can be determined using these three equations.

2.E. Cosine-based transition smoothing

To enforce the smoothness of the transition region, the measured data $g_{\lambda,v}(u)$ and the extrapolation data $\widetilde{g}_{\lambda,v}(u)$ are combined by a cosine-like smooth weighting function in a predefined transition interval. The range of the transition interval is empirically determined as 1/30 of the number of the pixels at the measured projection row. For the right side of truncated image for instance, the transition interval is $[u_{\mathrm{trans}}, u_t]$ and the extrapolated values in this transition interval can be computed as follows:

$$g^{\mathrm{trans}}_{\lambda,v}(u) = g_{\lambda,v}(u)\cdot(1-\omega(u)) + \widetilde{g}_{\lambda,v}(u)\cdot\omega(u), \tag{20}$$

with the weight function $\omega(u)$ given by

$$\omega(u) = \frac{1}{2} + \frac{1}{2}\cos\left(\pi\frac{u-u_t}{u_t-u_{\mathrm{trans}}}\right), \tag{21}$$

where $\widetilde{g}_{\lambda,v}(u)$ indicates the extrapolated data by using either method proposed in Secs. 2.C or 2.D. Figure 5 shows a comparison of an extrapolated line with and without applying the cosine smoothing in the transition region.

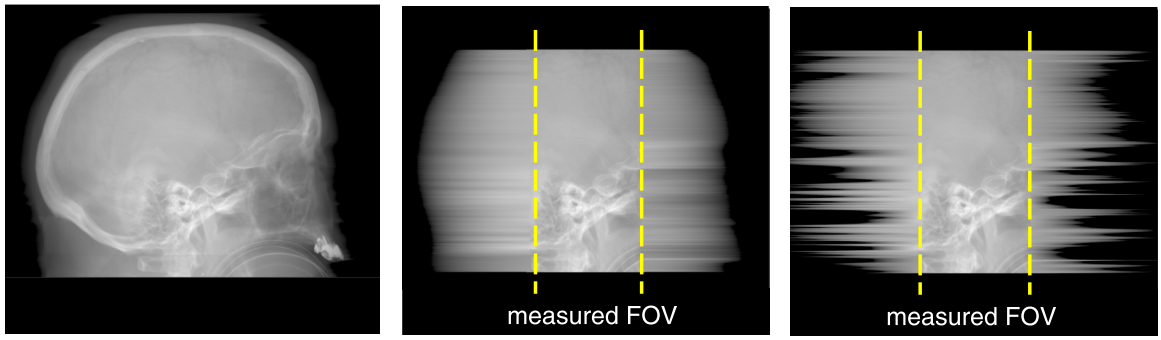

FIG. 7. Comparison of a nontruncated projection (left), a laterally truncated projection after applying the patient-bounded extrapolation (middle) and after the conventional water cylinder extrapolation (right).

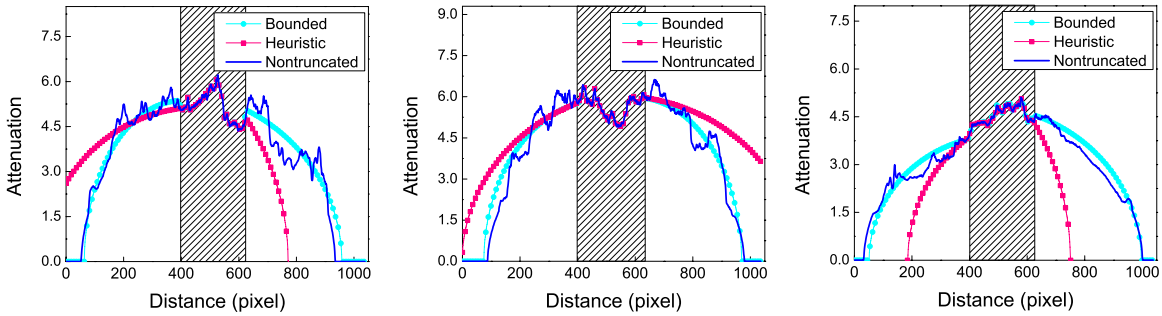

FIG. 8. Comparison of the nonbounded traditional extrapolation and patient-bounded extrapolation in a severe truncation case. Line profiles at projection views of $\lambda = -40°$ (left), $\lambda = 20°$ (middle), and $\lambda = 80°$ (right). Note that the bounded ellipse parameters are estimated using two single projections from $\lambda = -90°$ (ML) and $\lambda = 0°$ (AP). The shaded regions indicate the measured part of projections in VOI scan.

3. EVALUATION

3.A. Experiment setup

The proposed method was validated and evaluated on eight clinical head datasets (data courtesy of Street Luke's Episcopal Hospital, Houston, TX, and Rush University Medical Center, Chicago, IL). All datasets were acquired on a C-arm system with 496 projection images (1240×960 px) at a resolution of 0.308 mm/px. Even though a practical implementation would involve the extraction of the patient boundaries from low-dose fluoroscopic data, for proof of concept, we here confined to extract the boundaries from two projections ($\lambda = -90°$ and $\lambda = 0°$) of a noncollimated 3D scan. All datasets were virtually collimated (by setting the area outside region of interest to zeros) to a medium FOV (in a diameter of 80 mm in the volume domain) and a small FOV (in a diameter of 45 mm). The reconstruction results are onto a volume of 512^3 with an isotropic voxel size of 0.4 mm^3.

3.B. Reference methods

The standard FDK reconstruction[16] of nontruncated data is used as the reference for both qualitative and quantitative evaluation in each clinical case. The original, nonbounded water cylinder extrapolation (Hsieh *et al.*[3]) was investigated as a baseline and compared to our proposed algorithm for the two extrapolation schemes (Secs. 2.C and 2.D).

Suppose, the patient outline is exactly known from all projections, instead of only two. This could be potentially realized by deploying an optical tracking system (e.g., surface camera) to capture the patient outline and transform the outline in the C-arm coordinate system.[24] In this manner, the extrapolation scheme could be improved by incorporating a more accurate patient boundary information. We refer to this method as camera-based extrapolation. In this paper, we simulate this camera-based extrapolation method by ending the extrapolation lines at the boundary position detected from nontruncated projections. Note that this simulation is ideal in a sense that it does not account for some practical issues, e.g., inaccuracies caused by camera occlusions or potential errors that may be introduced by coregistration/calibration of the optical tracking system to the C-arm system.

3.C. Image quality metrics

To quantify image quality, three quantitative metrics were used: the root mean square error (RMSE), the relative root mean square error (rRMSE) (i.e., the RMSE divided by the total intensity range), and the correlation coefficient (CC). These image quality metrics are computed by using the reference FDK reconstruction from nontruncated data as reference over the entire VOI region.

3.D. Results

An example of the estimated ellipse model (only every tenth row is visualized) compared to the actual head phantom shape extracted from a FDK reconstruction on nontruncated data is shown in Fig. 6. Although fine shape details could not be preserved, the rough outline of the object is nicely

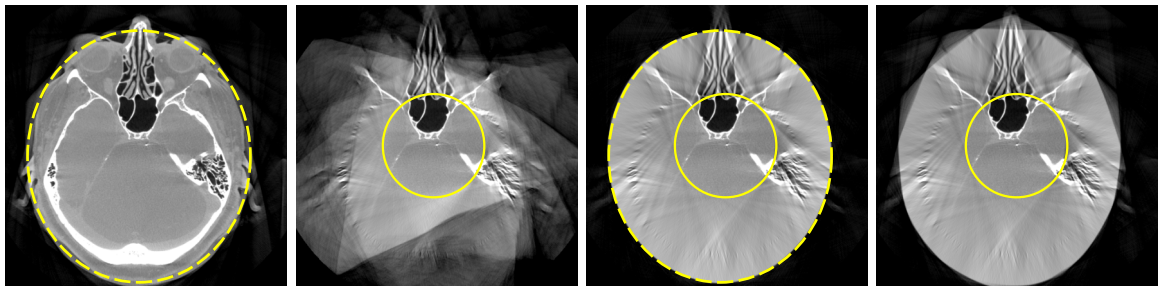

FIG. 9. Comparison of (from left to right) the FDK reconstruction from nontruncated projection data, VOI reconstruction corrected by the conventional water cylinder extrapolation, VOI reconstruction from truncated data corrected by the proposed method, and VOI reconstruction from truncated data corrected by the camera-based method. The dashed ellipses indicate the estimated outline of the patient and solid circles indicate the ROI.

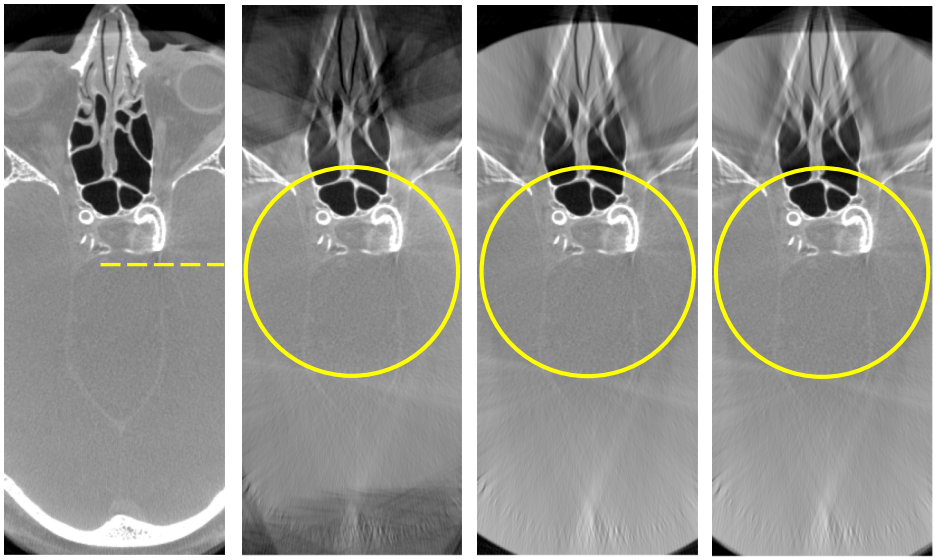

FIG. 10. Transversal slices of clinical data 1 (medium truncation) reconstructed by (from left to right): FDK on nontruncated data, heuristic water cylinder extrapolation, patient-bounded extrapolation, and camera-based extrapolation in the grayscale window [−1000,1000]. The yellow circles indicate the ROI.

described in the 3D ellipse model (see the similarity of the curvature of the back of the head).

Figure 7 shows a comparison of a nontruncated projection, a laterally truncated projection after applying the proposed extrapolation scheme and after conventional heuristic-based water cylinder extrapolation. The line profiles of the extrapolated projections over projection views of $\lambda = -40°$, $\lambda = 20°$, and $\lambda = 80°$ are presented in Fig. 8. We can see that since water cylinder extrapolation solely relies on local continuity at the truncation boundary, there is no guarantee that extrapolation lines will describe the real outline of the patient. On the other hand, the proposed bounded extrapolation (Sec. 2.C) fits the data outside the measured FOV more accurately, even for projections that differ from AP and ML view and in case of severe truncation. Similar observations can also be obtained in the reconstruction slices. From Fig. 9, we can see that the fitted ellipse estimated by the proposed method more describes the real object support (see the dashed ellipse) than the conventional extrapolation scheme, even though only VOI is of diagnostic interest.

More reconstruction results using different truncation correction methods from more different datasets are presented in Figs. 10–13, respectively. Comparison of the line profiles indicated as the dashed line in the slices is shown in Fig. 14. The quantitative evaluations for medium truncation and for severe truncation are summarized in Tables I and II, respectively. For visual inspection in the medium truncation case, the heuristic-based water cylinder extrapolation and patient-bounded methods (bounded water cylinder extrapolation and camera-based approach) avoid cupping-like trunca-

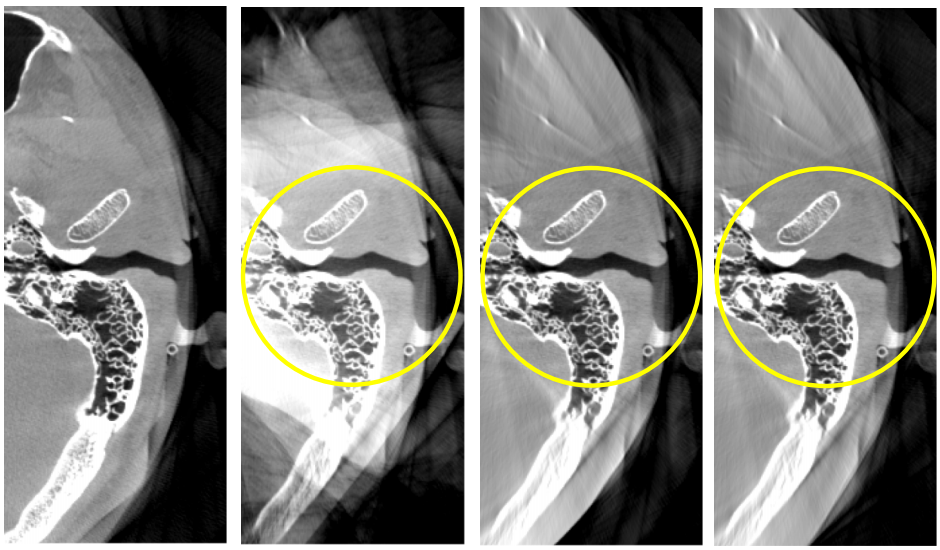

FIG. 11. Transversal slices of clinical data 2 (off-centered VOI, medium truncation) reconstructed by (from left to right): FDK on nontruncated data, heuristic water cylinder extrapolation, patient-bounded extrapolation, and camera-based extrapolation in the grayscale window [−1000,1000]. The yellow circles indicate the ROI.

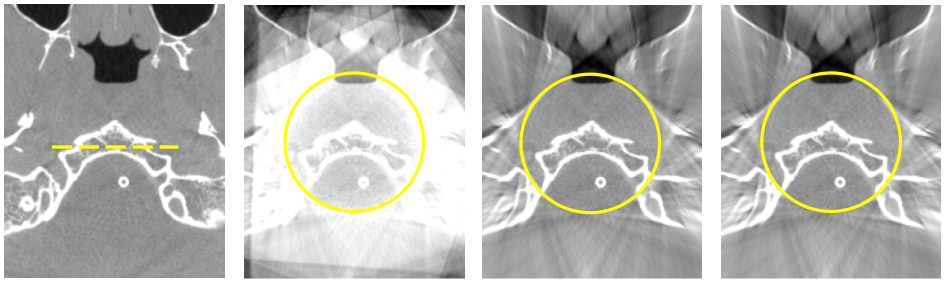

FIG. 12. Transversal slices of clinical data 3 (severe truncation) reconstructed by (from left to right): FDK on nontruncated data, heuristic water cylinder extrapolation, patient-bounded extrapolation, and camera-based extrapolation in the grayscale window [−1000,1000]. The yellow circles indicate the ROI.

tion artifacts and produce acceptable reconstruction results. The portions of the patient inside the FOV are visually comparable to the reference FDK reconstruction, see Fig. 10. The line profiles shown in Fig. 14 (top) confirm this observation, although water cylinder extrapolation exhibits a slight intensity increase close to the truncation boundary.

However, it becomes more challenging to the correction algorithms when it comes to an off-centered VOI case or severe truncation case. The water cylinder extrapolation yields truncation-induced cupping and large offset on gray values; see Fig. 11 for an off-centered VOI case and Figs. 12 and 13 for severe truncation case. These truncation artifacts can also be clearly observed from the line profile of the water cylinder extrapolation [see Fig. 14 (bottom)]. In contrast, the proposed method is still robust to these particular truncation cases. It is also interesting to see that the proposed patient-bounded extrapolation yields visually comparable results to that of camera-based extrapolation scheme, even though the 3D shape model of the former method is only estimated from two projection views.

Quantitative accuracy is improved considerably by the proposed method: the average RMSE reached as little as 34.4 gray values in the case of the medium truncation, compared to 139.9 from the heuristic water cylinder extrapolation. In the severe truncation case, the water cylinder extrapolation reconstruction is of substantially degraded quality image (RMSE of 420.4), due to the residual truncation artifacts, while the proposed method still retains a reconstruction of high quality (RMSE of 54.9). In terms of rRMSE, a relative error of about 1% was achieved by the proposed method, yielding an error reduction by a factor of 8 compared the heuristic water cylinder extrapolation method. Consistent with the visual inspection, the camera-based extrapolation is slightly superior to the proposed method (RMSE of 30.4

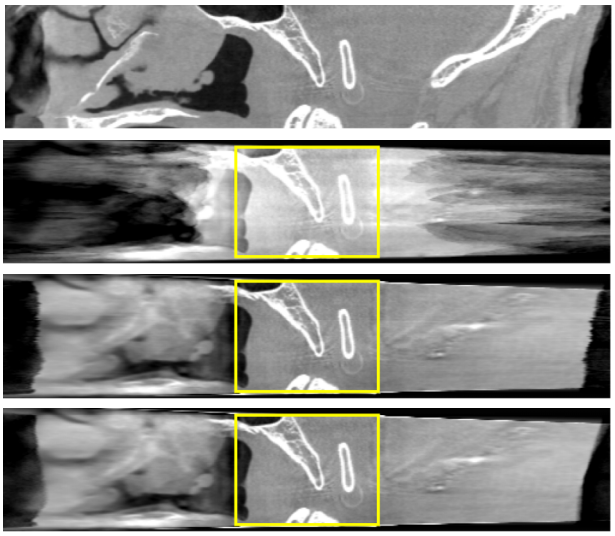

FIG. 13. Sagittal slices of clinical data 3 (severe truncation) reconstructed by (from top to bottom): FDK on nontruncated data, heuristic water cylinder extrapolation, patient-bounded extrapolation, and camera-based extrapolation in the grayscale window [−1000,1000]. The yellow rectangles indicate the ROI.

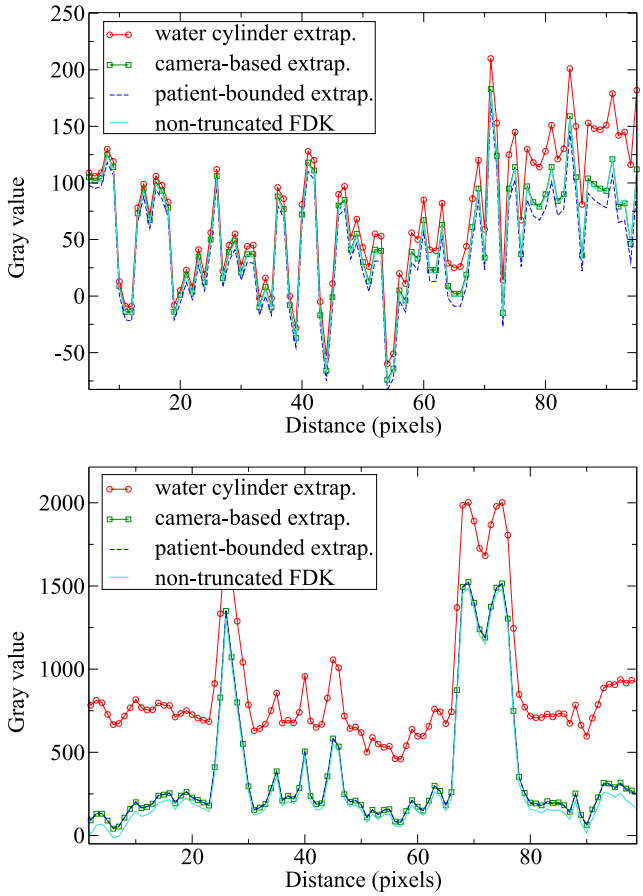

FIG. 14. Plots of line profile (indicated as the dashed line in the transversal slice) for each algorithm in the medium truncation case (top) and in the severe truncation case (bottom).

TABLE I. Quantitative evaluation of the different truncation corrections for the medium scan FOV. Note that the given RMSE, rRMSE, and CC are the average over all eight datasets.

	Water cylin.[a]	Bounded water cylin.	Bounded sqr.	Camera based
RMSE	139.9 ± 70.8	34.4 ± 15.0	53.4 ± 21.8	30.4 ± 11.0
rRMSE (%)	2.48 ± 1.36	0.67 ± 0.41	1.00 ± 0.61	0.58 ± 0.30
CC	0.945 ± 0.044	0.994 ± 0.003	0.993 ± 0.004	0.995 ± 0.002

[a]cf. heuristic water cylinder extrapolation from Ref. 3

gray values vs 34.4 gray values in medium truncation and 50.8 gray values vs 54.9 gray values in severe truncation). The correlation coefficients for both methods always achieve 0.99.

4. DISCUSSION

The method we proposed in this paper leads to a major improvement in image quality for 3D C-arm based VOI imaging, compared to the purely heuristic-based extrapolation methods.[2–6] Experimental results underline that this particularly applies for severe truncation case. As opposed to the algorithms suggested in Refs. 12–14, the proposed method involves no additional radiation when using the fluoroscopic images that are acquired anyway during the patient isocentering process. The model estimation can be readily integrated into the existing interventional workflow without additional hardware. Furthermore, the newly proposed method poses little constraints on the availability of prior image data such as preoperative scans[7–9] collected during the intervention. Any such constraint would immediately imply a restriction of the applicability of the algorithm to a workflow that provides exactly the required data. There may also be a delay caused by registration of the patient. Although interior tomography yields a theoretically exact localized reconstruction from fully truncated data, both the POCS method and TV based compressed sensing are computationally expensive.[21] Therefore, these iterative methods do not meet the requirement for interventional use. Regarding computation times of the proposed method, slice-wise ellipse fitting and patient boundary estimation are computationally efficient since only the boundary points are involved with small vector/matrix multiplications. For proof of concept, a CPU implementation of our method was executed on one core of a 2.20 GHz CPU, yielding only 7 s additional time with respect to the standard water cylinder implementation[3] for reconstruction of the severely truncated projections using the same configuration described in Sec. 3.A.

The proposed method is well-suited for neurointerventions since: (1) the ellipse is a good model for the head and (2) the low-dose fluoroscopic images are usually noncollimated and cover the entire object of interest. Also, the current extrapolation scheme is based on stretch or shrink of the initial extrapolation line so that it ends at the precomputed boundary. Future work could involve the integration of the known anatomical structures, e.g., high density skull. To this end, we could first generate an anatomy atlas from various investigated patient skulls. Then, we perform a registration on the representative atlas image in order to align it to the measured fluoroscopic images. Finally, by incorporating the registered skull atlas into the 3D ellipse model, the extrapolation lines may approximate the missing measurements in a more accurate manner.

A limitation of the proposed method is that the imaged object should be fully covered in the fluoroscopic images from both views. Note that this requirement may not be fulfilled for a body scan due to limited size of the flat detector in a C-arm system. For this proof of concept study, we used a global threshold to extract patient outlines from the two projections. This may not be feasible in a clinical setting when objects such as the patient bed or head support are present in the scan FOV. In this case, more advanced segmentation techniques are needed.

The evaluation results showed that the 3D shape model estimated by only two perpendicular views yields reconstructions of high accuracy. It is qualitatively and quantitatively comparable to the camera-based extrapolation in which the patient outline is known from all projections. Currently, we only incorporated the exploited patient boundary information into the water cylinder extrapolation[3] and the square root function extrapolation.[4] But, theoretically, this information can also be applied to other extrapolation schemes.[2,5,6] From the quantitative evaluation, we can see that patient-bounded water cylinder extrapolation performs better than patient-bounded square root extrapolation in the medium truncation case. This is because when the truncation is mild, the stretched or shrinked extrapolation lines from a water

TABLE II. Quantitative evaluation of the different truncation corrections for the small scan FOV. Note that the given RMSE, rRMSE, and CC are the average over all eight datasets.

	Water cylin.	Bounded water cylin.	Bounded sqr.	Camera based
RMSE	420.4 ± 88.9	54.9 ± 22.3	57.7 ± 19.9	50.8 ± 15.9
rRMSE(%)	8.02 ± 3.01	1.04 ± 0.55	1.05 ± 0.34	0.95 ± 0.43
CC	0.899 ± 0.040	0.991 ± 0.006	0.990 ± 0.007	0.992 ± 0.004

cylinder model fit the missing data better than a square root function. However, in case of severe truncation, the two approaches become comparable. Therefore, it would be also interesting to incorporate the patient boundary information into other extrapolation techniques and compare their performance.

ACKNOWLEDGMENTS

The authors gratefully acknowledge funding by Siemens AG, Healthcare Sector and of the Erlangen Graduate School in Advanced Optical Technologies (SAOT) by the German Research Foundation (DFG) in the framework of the German excellence initiative. The concepts and information presented in this paper are based on research and are not commercially available.

APPENDIX: DETERMINATION OF THE CLOSEST POINT OF TWO 3D LINES

To compute the closest point of two 3D lines $\mathbf{l}_m^{\mathrm{AP}}$ and $\mathbf{l}_m^{\mathrm{ML}}$, we establish $\mathbf{l}_m^{\mathrm{AP}}(t) = \mathbf{l}_m^{\mathrm{ML}}(l)$ and solve for t,

$$
\begin{aligned}
&\mathbf{l}_m^{\mathrm{AP}}(t) = \mathbf{l}_m^{\mathrm{ML}}(l),\\
&\mathbf{s}^{\mathrm{AP}} + t\mathbf{e}_m^{\mathrm{AP}} = \mathbf{s}^{\mathrm{ML}} + l\mathbf{e}_m^{\mathrm{ML}},\\
&t\mathbf{e}_m^{\mathrm{AP}} = \mathbf{s}^{\mathrm{ML}} - \mathbf{s}^{\mathrm{AP}} + l\mathbf{e}_m^{\mathrm{ML}},\\
&t\mathbf{e}_m^{\mathrm{AP}} \times \mathbf{e}_m^{\mathrm{ML}} = \left(\mathbf{s}^{\mathrm{ML}} - \mathbf{s}^{\mathrm{AP}}\right) \times \mathbf{e}_m^{\mathrm{ML}} + l\mathbf{e}_m^{\mathrm{ML}} \times \mathbf{e}_m^{\mathrm{ML}},\\
&t\left(\mathbf{e}_m^{\mathrm{AP}} \times \mathbf{e}_m^{\mathrm{ML}}\right) = \left(\mathbf{s}^{\mathrm{ML}} - \mathbf{s}^{\mathrm{AP}}\right) \times \mathbf{e}_m^{\mathrm{ML}} + l\mathbf{0},\\
&t\left(\mathbf{e}_m^{\mathrm{AP}} \times \mathbf{e}_m^{\mathrm{ML}}\right) \cdot \left(\mathbf{e}_m^{\mathrm{AP}} \times \mathbf{e}_m^{\mathrm{ML}}\right) = \left(\left(\mathbf{s}^{\mathrm{ML}} - \mathbf{s}^{\mathrm{AP}}\right) \times \mathbf{e}_m^{\mathrm{ML}}\right) \cdot \left(\mathbf{e}_m^{\mathrm{AP}} \times \mathbf{e}_m^{\mathrm{ML}}\right),\\
&t = \frac{\left(\left(\mathbf{s}^{\mathrm{ML}} - \mathbf{s}^{\mathrm{AP}}\right) \times \mathbf{e}_m^{\mathrm{ML}}\right) \cdot \left(\mathbf{e}_m^{\mathrm{AP}} \times \mathbf{e}_m^{\mathrm{ML}}\right)}{\left\|\mathbf{e}_m^{\mathrm{AP}} \times \mathbf{e}_m^{\mathrm{ML}}\right\|^2}.
\end{aligned}
$$

[a]Also with the Erlangen Graduate School in Advanced Optical Technologies (SAOT), Erlangen, Germany.

[1]G. T. Herman and R. M. Lewitt, "Evaluation of a preprocessing algorithm for truncated ct projections," J. Comput. Assisted Tomogr. **5**, 127–135 (1981).
[2]B. Ohnesorge, T. Flohr, K. Schwarz, J. P. Heiken, and J. P. Bae, "Efficient correction for CT image artifacts caused by objects extending outside the scan field of view," Med. Phys. **27**(1), 39–46 (2000).
[3]J. Hsieh, E. Chao, J. Thibault, B. Grekowicz, A. Horst, S. McOlash, and T. J. Myers, "A novel reconstruction algorithm to extend the CT scan field-of-view," Med. Phys. **31**(9), 2385–2391 (2004).
[4]K. Sourbelle, M. Kachelriess, and W. A. Kalender, "Reconstruction from truncated projections in CT using adaptive detruncation," Eur. Radiol. **15**(5), 1008–1014 (2005).
[5]B. Zellerhoff, B. Scholz, E. P. Ruehrnschopf, and T. Brunner, "Low contrast 3D-reconstruction from C-arm data," Proc. SPIE **5745**, 646–655 (2005).
[6]J. D. Maltz, S. Bose, H. P. Shukla, and A. R. Bani-Hashemi, "CT truncation artifact removal using water-equivalent thicknesses derived from truncated projection data," in *IEEE Engineering in Medicine and Biology Society* (IEEE EMBS, Lyon, 2007), pp. 2905–2911.
[7]K. J. Ruchala, G. H. Olivera, J. M. Kapatoes, R. J. Reckwerdt, and T. R. Mackie, "Methods for improving limited field-of-view radiotherapy reconstructions using imperfect a priori images," Med. Phys. **29**, 2590–2605 (2002).
[8]J. Wiegert, M. Bertram, T. Netsch, J. Wulff, J. Weese, and G. Rose, "Projection extension for region of interest imaging in cone-beam CT," Acad. Radiol. **12**, 1010–1023 (2005).
[9]D. Kolditz, Y. Kyriakou, and W. A. Kalender, "Volume-of-interest (VOI) imaging in C-arm flat-detector CT for high image quality at reduced dose," Med. Phys. **37**(6), 2719–2730 (2010).
[10]K. Sen Sharma, C. Holzner, D. M. Vasilescu, X. Jin, S. Narayanan, M. Agah, E. A. Hoffman, H. Yu, and G. Wang, "Scout-view assisted interior micro-CT," Phys. Med. Biol. **58**, 4297–4314 (2013).
[11]H. Yu, G. Cao, L. Burk, Y. Lee, J. Lu, P. Santago, O. Zhou, and G. Wang, "Compressive sampling based interior reconstruction for dynamic carbon nanotube micro-CT," J. Xray. Sci. Technol. **17**, 295–303 (2009).
[12]R. Chityala, K. R. Hoffmann, D. R. Bednarek, and S. Rudin, "Region of interest (ROI) computed tomography," Proc. SPIE **5368**(2), 534–541 (2004).
[13]L. Chen, C. C. Shaw, M. C. Altunbas, C. J. Lai, X. Liu, T. Han, T. Wang, W. T. Yang, and G. J. Whitman, "Feasibility of volume-of-interest (VOI) scanning technique in cone beam breast CT – A preliminary study," Med. Phys. **35**(8), 3482–3490 (2008).
[14]S. Schafer, P. B. Noel, A. Walczak, and K. Hoffmann, "Filtered region of interest cone-beam rotational angiography," Med. Phys. **37**(2), 694–703 (2010).
[15]F. Dennerlein and A. Maier, "Approximate truncation robust computed tomography - ATRACT," Phys. Med. Biol. **58**, 6133–6148 (2013).
[16]L. A. Feldkamp, L. C. Davis, and J. W. Kress, "Practical cone beam algorithm," J. Opt. Soc. Am. A **1**, 612–619 (1984).
[17]Y. Xia, F. Dennerlein, S. Bauer, H. Hofmann, J. Hornegger, and A. Maier, "Scaling calibration in region of interest reconstruction with the 1D and 2D ATRACT algorithm," Int. J. Comput. Assisted Radiol. Surg. **9**, 345–356 (2014).
[18]Y. Ye, H. Yu, and G. Wang, "Exact interior reconstruction from truncated limited-angle projection data," Int. J. Biomed. Imaging **2008**, 1–6.
[19]H. Kudo, M. Courdurier, F. Noo, and M. Defrise, "Tiny a priori knowledge solves the interior problem in computed tomography," Phys. Med. Biol. **52**(9), 2207–2231 (2008).
[20]H. Yu and G. Wang, "Compressed sensing based interior tomography," Phys. Med. Biol. **54**(9), 2791–2805 (2009).
[21]H. Yu, G. Wang, J. Hsieh, D. W. Entrikin, S. Ellis, B. Liu, and J. J. Carr, "Compressive sensing-based interior tomography: Preliminary clinical application," J. Comput. Assisted Tomogr. **35**, 762–764 (2011).
[22]J. Yang, W. Cong, M. Jiang, and G. Wang, "Theoretical study on high order interior tomography," J. X-Ray Sci. Technol. **20**, 423–436 (2012).
[23]E. Katsevich, A. Katsevich, and G. Wang, "Stability of the interior problem with polynomial attenuation in the region of interest," Inverse Probl. **28**, 065022 (2012).
[24]D. Kolditz, M. Meyer, Y. Kyriakou, and W. A. Kalender, "Comparison of extended field-of-view reconstructions in C-arm flat-detector CT using patient size, shape or attenuation information," Phys. Med. Biol. **56**(1), 39–56 (2011).